Materials Science in Semiconductor Processing 16 (2013) 612–618

Contents lists available at SciVerse ScienceDirect

Materials Science in Semiconductor Processing

journal homepage: www.elsevier.com/locate/mssp

Fabrication and characterization of $Pb_{1-x}Yb_xTe$-based alloy thin-film thermoelectric generators grown by thermal evaporation technique

A. Hmood [a,b,*], A. Kadhim [a,b], H. Abu Hassan [a]

[a] Nano-Optoelectronic Research and Technology Laboratory (N.O.R.), School of Physics, Universiti Sains Malaysia, 11800 USM, Penang, Malaysia

[b] Department of Physics, College of Science, University of Basrah, Basrah, Iraq

ARTICLE INFO

Available online 21 December 2012

Keywords:
Thermal evaporation method
Thin films
Thermoelectric generators

ABSTRACT

In this study p-$Pb_{0.925}Yb_{0.075}Te$:Te and n-$Pb_{0.94}Yb_{0.06}Te$ powders synthesized by solid-state microwave technique were used to fabricate thermally evaporated thin films. The nanostructure and composition of the films were studied using X-ray diffraction (XRD), field emission scanning electron microscopy (FESEM) and energy dispersive X-ray spectroscopy (EDX). Electrical characterizations of the as-deposited films in terms of the Seebeck coefficient and electrical conductivity and power factor were conducted at a range of 298 K to 523 K. The microthermoelectric devices were composed of 20-pair and 10-pair p-$Pb_{0.925}Yb_{0.075}Te$:Te and n-$Pb_{0.94}Yb_{0.06}Te$ thin films on glass substrates. The dimensions of the thin-film thermoelectric generators, which consisted of 20-pair and 10-pair legs connected by aluminum electrodes, were 23 mm × 20 mm and 12 mm × 10 mm, respectively. The 20-pair p–n thermocouples in series generated a maximum open-circuit voltage output (V_{oc}) of 0.581 V and a maximum output power of 25.87×10^{-8} W at a temperature difference $\Delta T = 164$ K, whereas the 10-pair p–n thermocouples generated 0.311 V and 13.71×10^{-8} W maximum V_{oc} and maximum output power, respectively, at $\Delta T = 164$ K.

1. Introduction

Interest in local cooling and low-power energy-scavenging applications have grown in the last decade. These applications have been used to generate a few microwatts of power at relatively high voltage to power small electronic devices, wireless sensors, wearable electronics, and other industrial heat-generating processes [1,2]. A combination of recent significant advances in the scientific understanding of quantum wells, nanostructure effects on thermoelectric (TE) properties, and modern thin-layer and nanoscale manufacturing technologies have created advanced TE materials with potential conversion efficiencies of over 15% [3]. The advent of these advanced TE materials offers new opportunities to recover waste heat more efficiently and economically with highly reliable and relatively passive systems that eliminate noise and vibration [4,5]. A thermoelectric power generation (TEG) device produces voltage when a temperature difference (ΔT) occurs between the two sides of the device because of the thermoelectric effect (TE). TE includes the Seebeck (S), Peltier, and Thomson effects. TE is also associated with other effects, such as Joulean and Fourier effects [6,7]. TE generation has primarily been directed toward increasing the material figure of merit (ZT), which is the standard measure of the TE performance of a material, that is, $ZT = S^2\sigma T/\kappa$, where S is the Seebeck coefficient, σ the electrical conductivity, κ the thermal conductivity, and T the absolute temperature. $S^2\sigma$ is defined as the thermoelectric power factor [8]. The power factor should be maximized, whereas the thermal conductivity should be minimized to achieve a high-efficiency thermoelectric material. Earlier developments in microthermoelectric devices used thin-film

* Corresponding author. Tel.: +60142441397; fax: +6046579150.
E-mail address: arshad.phy73@gmail.com (A. Hmood).

1369-8001/$ - see front matter © 2012 Elsevier Ltd. All rights reserved.
http://dx.doi.org/10.1016/j.mssp.2012.11.006

depositions based on different growth methods, such as molecular beam epitaxy [9], electrochemical deposition [10], radio frequency co-sputtering [5,11], simple vacuum thermal evaporation [6], flash evaporation [2], and co-evaporation [4], to grow single layers and superlattices on various substrates [12]. The present study explored the design of thin films, the enhancement of microfabrication methods, and the related electrical characterizations to improve the performance and integration of microscale TE generators. A $Pb_{0.925}Yb_{0.075}Te$:Te alloy was prepared as p-type ingot, and a $Pb_{0.94}Yb_{0.06}Te$ alloy as n-type ingot by solid-state microwave for the fabrication of 20-pair and 10-pair thin-film thermoelectric microdevices, respectively (23 mm × 20 mm and 12 mm × 10 mm, respectively). This procedure was done via a thermal evaporation technique onto glass substrates. The intrinsic properties of each of the thin-film components were investigated. The output voltage (V_{out}) and the calculation of the maximum output power of a complete generator was measured within the temperature range of 298 K to 523 K, as functions of the temperature difference between the hot and cold junctions.

2. Experimental

The n-type $Pb_{0.94}Yb_{0.06}Te$ was synthesized as a ternary compound by standard solid-state microwave technique. A 2 g portion of the sample was prepared from three high-purity element powders (Pb; Te ≥ 99.999%, 100 meshes; and Yb ≥ 99.9%, 157 μm) based on the stoichiometric ratio $(1-x):x:1$ [13]. The polycrystalline alloys of p-type $Pb_{0.925}Yb_{0.075}Te$:Te was prepared by the same techniques after the addition of excess of Te. The thin films of the thermoelectric generators were then deposited onto clean glass substrates by thermal evaporation at 10^{-6} mbar and at room temperature using a silicon monoxide source (SO-20 series, R. D. Mathis Co., USA). The p-type ($Pb_{0.925}Yb_{0.075}$-Te:Te) and n-type ($Pb_{0.94}Yb_{0.06}Te$) powders were positioned in the load cavity of the boat. The vapors followed an indirect path through a series of baffles during heating and exited from a vertical chimney 12 mm in height and 6.3 mm in diameter. Thus, the substrates were not exposed to the bulk $Pb_{1-x}Yb_xTe$ material at any time, essentially eliminating any chance of spitting and streaming, which causes pinholes, as shown in Fig. 1. The distance between the tantalum boat and the substrate was 180 mm. The thicknesses of the thin films were approximately 0.947 μm, as determined using an optical reflectometer (Filmatric F20, USA). The patterned shadow masks

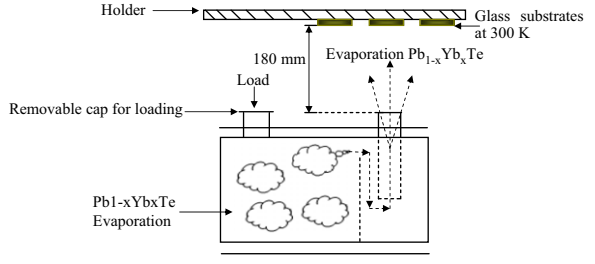

Fig. 1. Scheme of the silicon monoxide source used to prepare polycrystalline superlattice $Pb_{1-x}Yb_xTe$ thin films.

fabricated 20-pair and 10-pair thermoelectric microdevices (23 mm × 20 mm and 12 mm × 10 mm, respectively) for the p- and n-leg thin films and their junctions, respectively. The rectangular tracks on the glass substrates were 400 μm in width and 20 mm in length for the 20-pair p-legs and 400 μm and 10 mm for the 10-pair n-legs (Fig. 2(b)). The dimensions of the p- or n-legs were 20 mm or 10 mm (l) × 400 μm (w) × 0.947 μm (t), and the spacing between both leg types was 150 μm (Fig. 2). A diffusion barrier layer (Al electrode thickness is 420 nm) was sputtered between the p- and n-type thin films of the thermoelectric generator at the junctions. The crystal structure, surface morphology, and composition analysis of the semi-magnetic semiconductor lead–ytterbium–telluride thin films were examined by X-ray diffraction (XRD) using a PANalytical X'Pert PRO MRD PW3040 (Almelo, Netherlands) with Cu Kα radiation (λ=0.154060 nm), field emission scanning electron microscopy (FESEM), and energy dispersive X-ray spectroscopy (EDX, model Leo-Supra 50 VP, Carl Zeiss, Germany), respectively. The electrical conductivity and Seebeck coefficient of

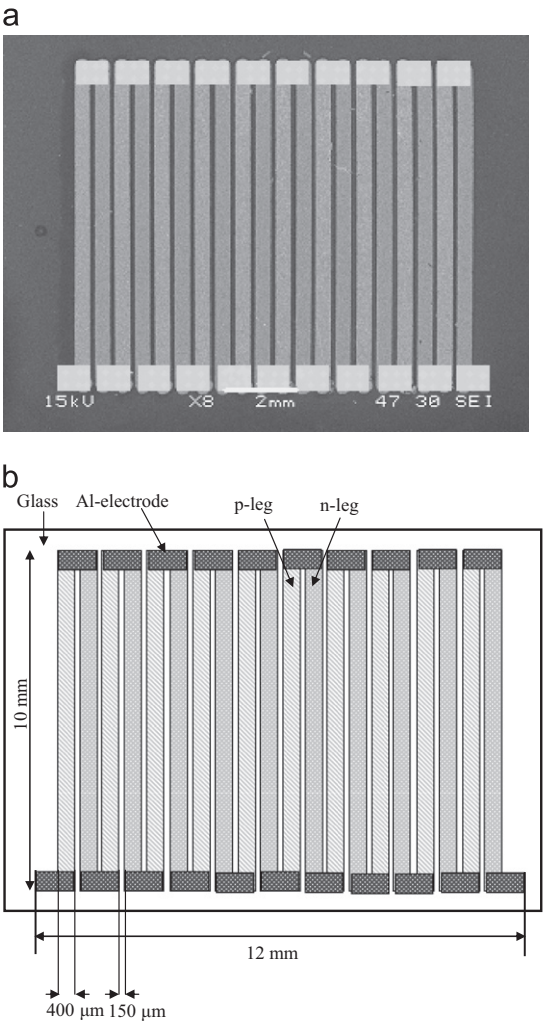

Fig. 2. (a) SEM images of the thin-film thermoelectric generator fabricated on glass substrate; and (b) schematic of the thin-film thermoelectric generator.

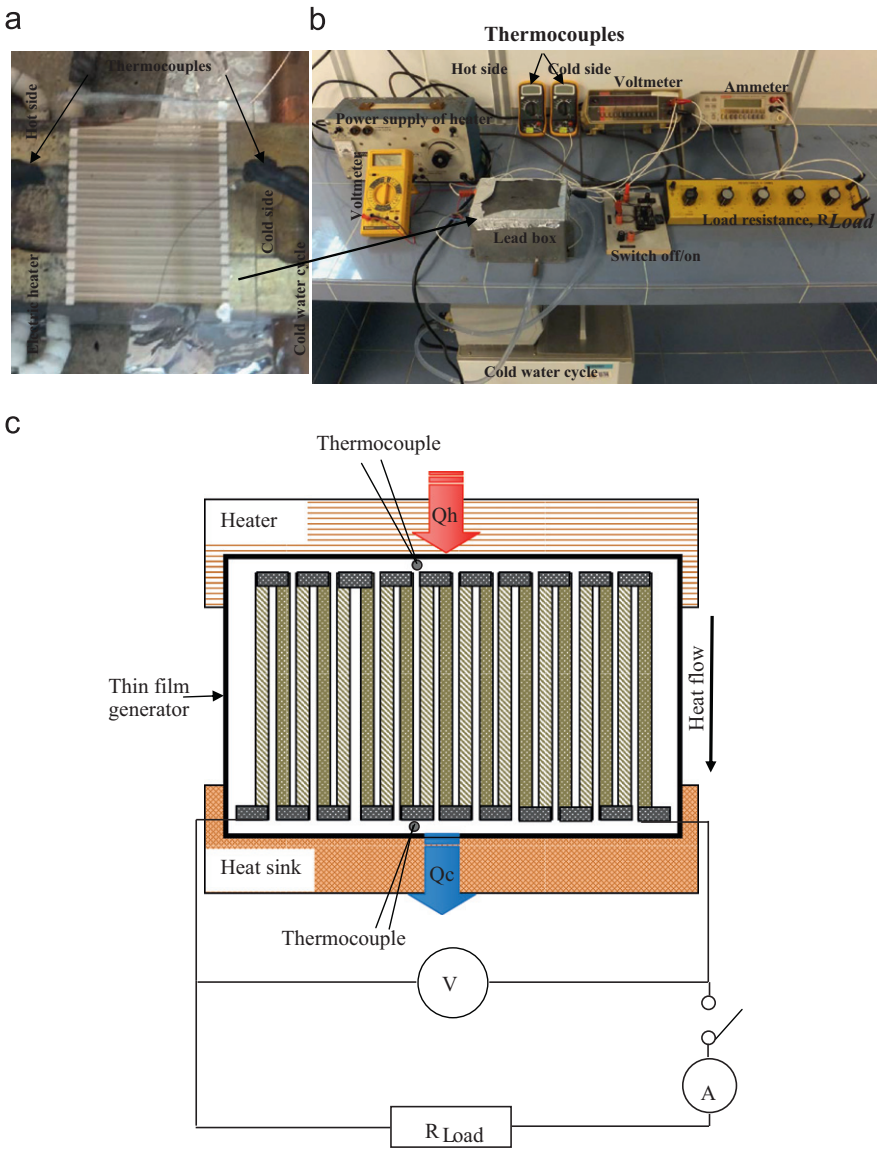

Fig. 3. (a) Photograph of 20-pair thin-film thermoelectric generator setup inside lead box; (b) experimental setup of the measurement of the output voltage (V_{out}) of the $Pb_{1-x}Yb_xTe$ alloy thin-film thermoelectric generators; and (c) schematic of the V_{oc} of the thin-film thermoelectric generators measured as functions of the temperature difference (ΔT) between the hot and cold junctions.

the thin films were measured within the temperature range of 298 K to 523 K at the two ends of the film. The thermal gradients were also measured in increments at both ends using two separate thermocouples (type-K E©Sun ECS820C) that were in direct contact with the films. The output voltage (V_{out}) of the thin-film thermoelectric generators was initially measured while imposing a temperature gradient of $\Delta T = T_h - T_c$ between the hot and cold junctions of the generators. Fig. 3 shows the experimental setup and the schematic for the measurement of V_{out}, output current (I_{out}), and internal resistance (R_{in}) of the thin-film thermoelectric generator. The V_{out} and I_{out} were measured at the Al electrode pads connected to the thermoelectric legs. The measurement pairs of the voltage and current were acquired, and the load resistance (R_{Load}) was manually adjusted. The R_{in} of the thin-film thermoelectric generators was also measured using a two-wire method. R_{in} was modified by the contact resistances, that is, $R_{in} = R_{in\text{-}ideal} + R_{contact}$, of the thermoelectric generator was calculated using $R_{in} = V_{oc}/I_{sc}$, where V_{oc} is the open-circuit voltage, and I_{sc} is the short-circuit current. The maximum output power of the thin-film thermoelectric generators was calculated from the V_{out} and the overall resistance of the generators.

3. Results and discussion

(200) oriented p-$Pb_{0.925}Yb_{0.075}Te$:Te and n-$Pb_{0.94}Yb_{0.06}Te$ thin films with cubic nanostructures were synthesized using the simple vacuum thermal evaporation technique,

which created a favorable growth environment for the films. Fig. 4 shows the XRD patterns of $Pb_{0.925}Yb_{0.075}Te$:Te and $Pb_{0.94}Yb_{0.06}Te$ films. In the $Pb_{0.925}Yb_{0.075}Te$:Te film, all peaks can be indexed as cubic PbTe with a face-centered, rock salt (NaCl)-type structure (JCPDS 38-1435). The calculated lattice constant $a=6.465$ Å was in good agreement with previous literature data of 6.449 Å [14], 6.453 Å [15], and 6.464 Å [16]. The slight increase in value was due to the change in the nature of the chemical bonding because of the substitution of Yb for Pb. Hence, being the most elongated of all, the Yb–Te distance is ~3% longer than the corresponding distance in YbTe (3.18 Å), and ~1.5% longer than Pb–Te distance in pure PbTe (3.23 Å) [17]. The FESEM images in Fig. 5 reveal the morphologies of the p-type and n-type thin films. The films were polycrystalline with a preferential crystallite orientation at (200). The numerous nanocubes of the Pb–Yb–Te material were clearly visible. In addition, the EDX spectra showed that the excess Te in $Pb_{0.925}Yb_{0.075}$-Te:Te was higher than the stoichiometric ratio for the $Pb_{0.925}Yb_{0.075}Te$ thin films without excess Te (Fig. 5). The actual weights (%) for the stoichiometric sample were experimentally determined equal to 41.56%, 1.69%, and 56.75% for Te, Yb, and Pb, respectively. Generally, compositions were considered as n- or p-type carrier concentrations, on the assumption that one excess Pb atom corresponds to one free electron, and that one excess Te atom corresponds to one free hole, respectively. This result agrees well with previous X-ray data for the p-$Pb_{1-x}Sn_xTe$:Te material (50.1 at% Te at 600 °C) [18,19].

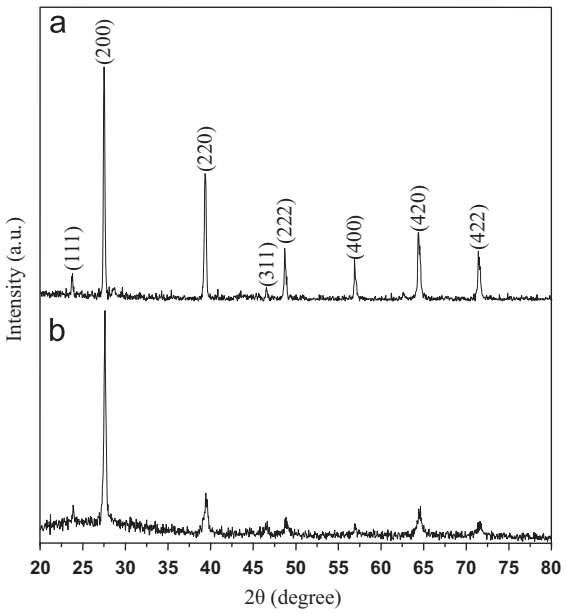

Fig. 4. XRD patterns of (a) p-$Pb_{0.925}Yb_{0.075}Te$:Te and (b) n-$Pb_{0.94}Yb_{0.06}Te$ as-deposited thin films.

The electrical characterizations of the as-deposited films in terms of electrical conductivity, the Seebeck coefficient, and the power factor were conducted between 298 K and 523 K (Fig. 6). The electrical conductivity (σ) of both types exhibited the same increased behavior with increasing temperature, indicating the semiconductor behavior of all alloys. The analysis of the σ behavior of both types revealed that the conduction mechanisms employ two different pathways with two different slopes, indicating the presence of two electronic transitions (Fig. 6(a)). The first electronic transition occurred in the low-temperature region between 3.3 K^{-1} and 2.6 K^{-1} (300 K to 383 K), whereas the other transition occurred in the high-temperature region between 2.26 K^{-1} and 1.9 K^{-1} (443 K to 523 K). The linearity of $\ln\sigma$ against $1/T$ for the low and high-temperature regions indicates that the

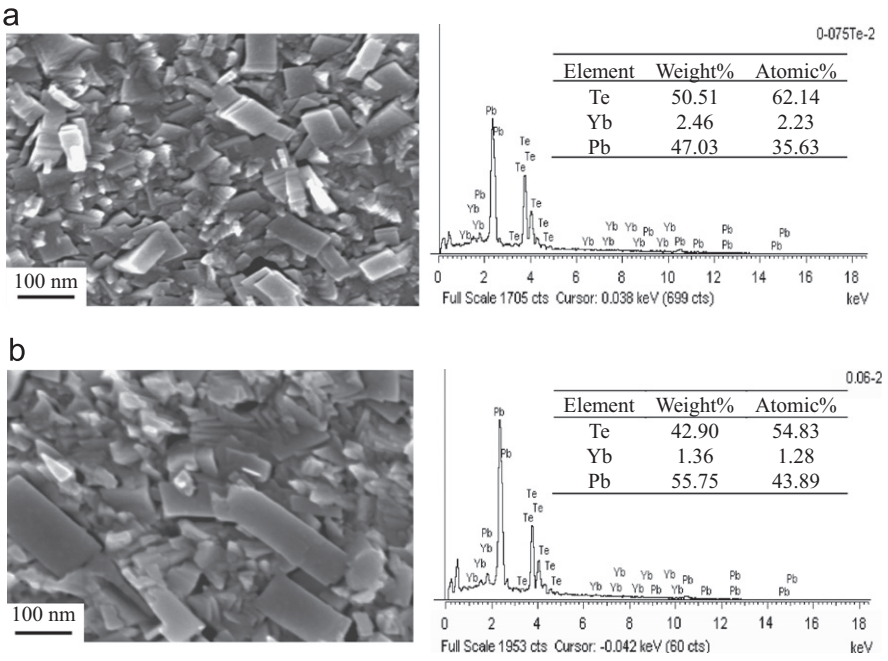

Fig. 5. FESEM images and EDX spectra of (a) p-$Pb_{0.925}Yb_{0.075}Te$:Te and (b) n-$Pb_{0.94}Yb_{0.06}Te$ as-deposited thin films.

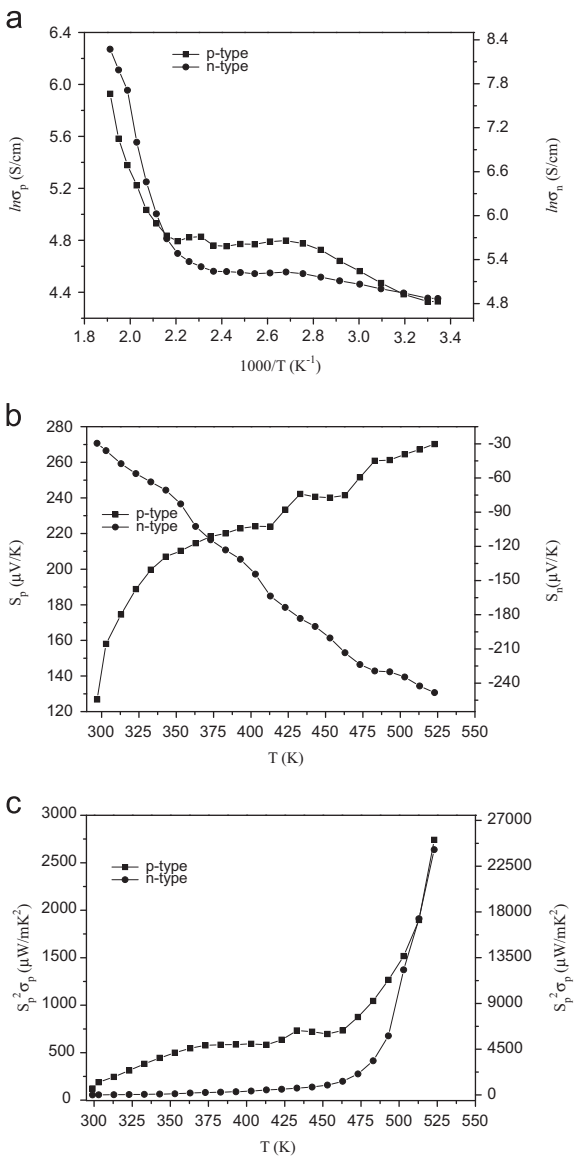

Fig. 6. Electrical transport properties of $Pb_{1-x}Yb_xTe$ thin films: (a) electrical conductivity; (b) Seebeck coefficient; and (c) power factor.

intrinsic conduction predominates. However, in the middle-temperature region between 2.42 K^{-1} and 2.36 K^{-1} (413 K to 423 K), the curves continuously decreased with increasing temperature, which is consistent with a degenerate semiconductor conduction caused by the formation of density of states near the Fermi level [20].

Fig. 6(b) shows the Seebeck coefficient ($S=\Delta V/\Delta T$) which was determined from the slope of the thermoelectric electromotive force versus the temperature difference between the hot and cold ends of the films. The Seebeck coefficient of the p-type film (S_p) was 270.24 μV/K, whereas n-type film (S_n) was −248.36 μV/K at 523 K, where the + or − signs indicate the type of carrier. Fig. 6(c) shows that the power factor $S^2\sigma$ for both types increased with increasing temperature range. The $S^2\sigma$ exhibited a behavior typical of semiconductors and significantly increased with increasing temperature, up to 523 K. This behavior is thus expected to be significant at high temperatures. The $S^2\sigma$ values for the n-type film were higher than those of the p-type films. The maximum value of $S_p^2\sigma_p$ was 2740.15 μW/mK^2, whereas that of $S_n^2\sigma_n$ was 24117.94 μW/mK^2 at 523 K.

Fig. 2 shows the fabricated microdevices of the p-$Pb_{0.925}Yb_{0.075}Te$:Te and n-$Pb_{0.94}Yb_{0.06}Te$ thin films. The films were dense and uniform as observed from the top view (SEM image of Fig. 2(a)). The performance of Pb–Yb–Te film-based microgenerators was investigated within the temperature range of 298 K to 532 K. ΔT was induced between the hot and cold junctions of the microgenerators. The V_{out} was measured versus the output current, output characteristic of the thermoelectric generators, and the maximum output power. Fig. 7 shows the load characteristics of the two microgenerators, namely, the V_{out} dependence, I_{out}, and P_{out} as functions of ΔT for (a) 20-pair and (b) 10-pair microgenerators. The V_{out} increased with increasing ΔT, and this conclusion is valid for the plot in Fig. 7 and for similar plots, considering the gradient temperatures in the thermoelectric generators were not behind a certain thermal saturation point.

A high linearity was observed in all V_{out} versus I_{out} plots and almost at the same slope. Thus, the $R_{in}=V_{oc}/I_{sc}$ of the thermoelectric generators was still consistent with the ΔT and R_{Load}. Therefore, the R_{in} of the analyzed

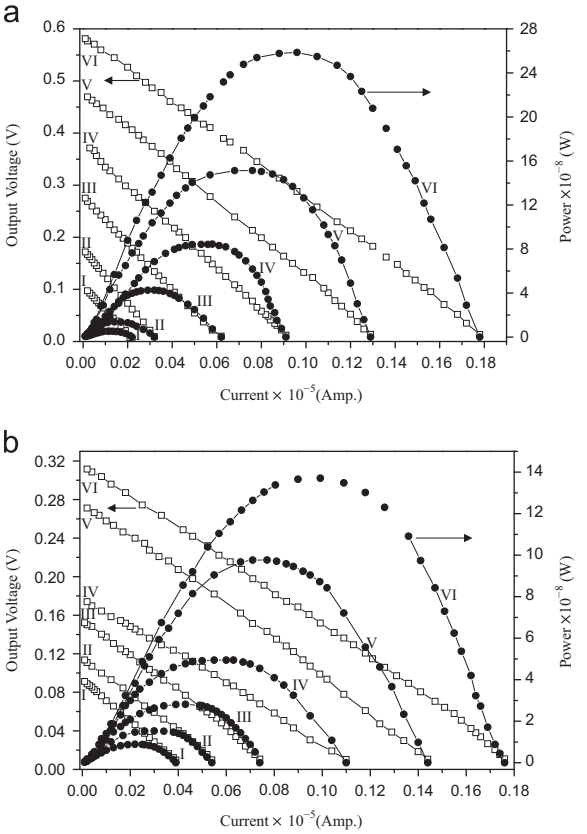

Fig. 7. Output power of the generators versus the output voltage and output current of (a) 20-pair and (b) 10-pair $Pb_{1-x}Yb_xTe$ microdevices with different ΔT: (I) $\Delta T=72$ K; (II) $\Delta T=92$ K; (III) $\Delta T=112$ K; (IV) $\Delta T=128$ K; (V) $\Delta T=146$ K; and (VI) $\Delta T=164$ K.

Table 1
Maximum open-circuit voltage (V_{oc}) and output power (P_{max}) at various ΔT for thin films thermoelectric generator.

Sample	ΔT (K)	72	92	112	128	146	164
10-pairs	V_{oc} (10^{-3} V)	91.22	113.53	152.12	173.98	271.2	311.6
	P_{max} (10^{-8} W)	0.89	1.53	2.81	4.94	9.76	13.71
20-pairs	V_{oc} (10^{-3} V)	97.47	171.76	275.2	371.3	469.4	581.3
	P_{max} (10^{-8} W)	0.54	1.4	4.27	8.45	15.14	25.87

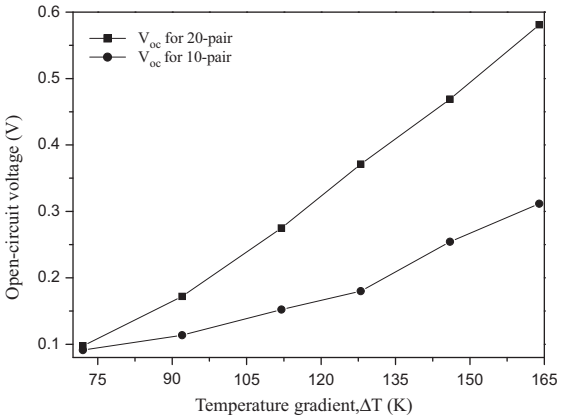

Fig. 8. Thin-film thermoelectric generator open-circuit output voltage V_{oc} various different temperature gradients ΔT.

thermoelectric devices are equal to 326.6 KΩ for the 20-pair and 177 KΩ for the 10-pair. An analysis of both plots in Fig. 7(a) and (b) reveals that P_{out} increases with the temperature gradient, indicating the rise in ΔT means an increase in V_{out} (Table 1). The higher the V_{out}, the higher the I_{out} and, considering several values were obtained for R_{Load}, the dissipated power will be in the external R_{Load} $\left(e.g., P_{out} = R_{Load} I_{out}^2\right)$. The alternative set of plots for the output power will be P_{out} versus the output current I_{out} (or versus R_{Load}). Fig. 7 illustrates six plots for the six different temperatures. However, an alternative set of plots was illustrated for the P_{out} versus V_{out} plots. The voltage or thermoelectric e.m.f. produced by the Seebeck effect is defined as $V_{out}=S_{p,n}\Delta T$, where $S_{p,n}$ indicates the relative Seebeck coefficient for a material pair p–n [11]. Several thermocouples were connected in series electrically and in parallel thermally with each other to form a thermopile, thereby maximizing the V_{out} generated. This method generated n times the V_{out} of one thermocouple (if n is the number of thermocouples in series) and a maximum output electric power with optimal impedance matching, which can be expressed as

$$P_{max} = \frac{(nS_{p,n}\Delta T)^2}{4R_{in}} \quad (1)$$

where P_{max} is the maximum output power and R_{in} is the internal electrical resistance of the generator.

The ideal $R_{in\text{-}ideal}$ is calculated from the thermocouple dimensions and the number of thermocouples in series, that is, $R_{in\text{-}ideal}=n(R_p+R_n)$ [21]. The maximum output power is presumably achieved when $R_{Load}=R_{in}$. Thus, the maximum output power of microgenerators were calculated as functions of the ΔT in the temperature region $\Delta T=164$ K [22]. Fig. 8 shows the experimental variation in the open-circuit voltage of thin-film thermoelectric generators that were measured as functions of the temperature difference between the hot and cold junctions. This result demonstrates that the devices have almost linear relationships with V_{oc} and ΔT. Thus, a minute amount of heat can be sensed by our device with a small ΔT, but generating a large V_{oc}. As reported, the prototype generates, at the temperature difference of 164 K, V_{oc} of 0.581 V and 25.87×10^{-8} W for 20-pair and 0.311 V and 13.71×10^{-8} W for 10-pair, respectively. These results are acceptable compared with those of other materials [5,12], considering V_{oc} and maximum output power were generated under a small ΔT. In fact, the thermoelectric generators were generally based on the Seebeck effect of heavily doped semiconductors that produce electrical energy [23–26]. In the thermoelectric generation, a more appropriate performance dynamic is the power factor, $S^2\sigma$ (W/K^2 m^{-1}). $S^2\sigma$ is defined as the electric power per unit area through which the heat flows per unit temperature gradient between the hot and the cold sides [25]. This condition is attributed to the microstructures that were not optimized and to the high contact resistance from the non-optimized bonding process [27]. The electrical and thermal contacts play important roles in improving the device power-generation performance and in minimizing other related contact problems.

4. Conclusion

Microscale $Pb_{1-x}Yb_xTe$ film-based microgenerators were successfully fabricated by thermal evaporation technique. The performance of the microgenerators was measured between 298 K and 523 K. The high V_{oc} of 0.581 V and 0.311 V and calculated output power of 25.87×10^{-8} W and 13.71×10^{-8} W, for 20 pairs and 10 pairs, respectively, were obtained with a $\Delta T=164$ K. The low power generated by each device geometry indicates inadequacy of these thermoelectric configurations in supplying high power. However, these devices are interesting enough as temperature sensors due to their effective voltage sensitivity. Therefore, the thermoelectric microdevices exhibit scalability in output power per unit volume. The power values were low, mainly because of the high electrical contact resistances of the chosen device geometry.

Acknowledgments

The authors are grateful for the funding provided by the Postgraduate Research Grant Scheme (PRGS) (No. 1001/PFIZIK/844134) of Universiti Sains Malaysia. We are also grateful to the Nano-Optoelectronics Research and Technology Laboratory (N.O.R.) of the School of Physics for the help extended during the research.

References

[1] M. Takashiri, T. Shirakawa, K. Miyazaki, H. Tsukamoto, Sensors and Actuators A 138 (2007) 329–334.
[2] G. Savelli, M. Plissonnier, J. Bablet, C. Salvi, J.M. Fournier, MEMS/MOEMS — DTIP, 2006, ISBN:2-916187-03-0.
[3] Kim Il-Ho, Materials Letters 43 (2000) 221–224.
[4] N.H. Bae, S. Han, K.E. Lee, B. Kim, S.-T. Kim, Current Applied Physics 11 (2011) S40–S44.
[5] N. Kaiwa, M. Hoshino, T. Yaginuma, R. Izaki, S. Yamaguchi, A. Yamamoto, Thin Solid Films 515 (2007) 4501–4504.
[6] M. Tan, Y. Wang, Y. Deng, Z. Zhang, B. Luo, J. Yang, Y. Xu, Sensors and Actuators A 171 (2011) 252–259.
[7] X. Niu, J. Yu, S. Wang, Journal of Power Sources 188 (2009) 621–626.
[8] D. Zhao, C. Tian, S. Tang, Y. Liu, L. Jiang, L. Chen, Materials Science in Semiconductor Processing 13 (2010) 221–224.
[9] G. Zeng, J.H. Bahk, J.E. Bowers, H. Lu, A.C. Gossard, S.L. Singer, A. Majumdar, Z. Bian, M. Zebarjadi, A. Shakouri, Applied Physics Letter 95 (2009) 083503.
[10] W. Glatz, S. Muntwyler, C. Hierold, Sensors and Actuators A 132 (2006) 337–345.
[11] L. Francioso, C. Pascali, I. De, Farella, C. Martucci, P. Creti, P. Siciliano, A. Perrone, Journal of Power Sources 196 (2011) 3239–3243.
[12] R. Izaki, M. Hoshino, T. Yaginuma, N. Kaiwa, S. Yamaguchi, A. Yamamoto, Microelectronics Journal 38 (2007) 667–671.
[13] A. Hmood, A. Kadhim, H. Hassan, Abu, Journal of Alloys and Compounds 520 (2012) 1–6.
[14] B. Wan, C. Hu, B. Feng, Y. Xi, X. He, Materials Science and Engineering B 163 (2009) 57–61.
[15] B. Wan, C. Hua, Y. Xi, J. Xu, X. He, Solid State Sciences 12 (2010) 123–127.
[16] X. Chen, T.-J. Zhu, X.-B. Zhao, Journal of Crystal Growth 311 (2009) 3179–3183.
[17] I. Radisavljevic, N. Novakovic, N. Romcevic, M. Manasijevic, H.E. Mahnke, N. Ivanovic, Journal of Alloys and Compounds 501 (2010) 159–163.
[18] G.T. Alekseeva, M.V. Vedernikov, E.A. Gurieva, L.V. Prokofeva, Yu.I. Ravich, Semiconductors 34 (2000) 897–901.
[19] N.V. Kolomoets, S.A. Laptev, E.I. Rogacheva, F.T. Poluprovodn, Semiconductor 20 (1986) 283.
[20] P.M. Nikolic, D. Lukovic, S.S. Vujatovic, K.M. Paraskevopoulos, M.V. Nikolic, V. Blagojevic, et al., Journal of Alloys and Compounds 466 (2008) 319–322.
[21] L. Han, Y. Jiang, S. Li, H. Su, X. Lan, K. Qin, T. Han, H. Zhong, L. Chen, D. Yu, Journal of Alloys and Compounds 509 (2011) 8970–8977.
[22] S.M. Choi, K.H. Lee, C.H. Lim, W.S. Seo, Energy Conversion and Management 52 (2011) 335–339.
[23] Y. Pei, A. La Londe, S. Iwanaga, G. Jeffrey Snyder, Environmental Science 4 (2011) 2085–2089.
[24] Yu I. Ravich, S.A. Nemov, Semiconductors 36 (2002) 1–20.
[25] H.S. Dow, M.W. Oh, B.S. Kim, S.D. Park, B.K. Min, H.W. Lee, D.M. Weel, Journal of Applied Physics 108 (2010) 113709.
[26] H. Wang, Y. Pei, A.D. La Londe, G. Jeffrey Snyder, Advanced Materials 23 (2011) 1366–1370.
[27] H.-B. Lee, H.J. Yang, J.H. We, K. Kim, K.C. Chol, B.J. Cho, Journal of Electronic Materials 40 (2011) 615–619.